

# Measurements of hypersonic double cone flows with shock wave/boundary layer interactions in the X3 expansion tunnel

Aaron Kennedy\* and Rowland Penty-Geraets†  
*University of Oxford, Oxford, Oxfordshire, OX2 0ES, UK*

Christopher M. James‡, Matthew Thompson§ and Richard G. Morgan¶  
*The University of Queensland, Brisbane, Queensland 4072, Australia*

Joanna M. Austin||  
*California Institute of Technology (GALCIT), Pasadena, California 91125*

Fabian Zander\*\*  
*University of Southern Queensland, Toowoomba, Queensland 4350, Australia*

Matthew McGilvray††  
*University of Oxford, Oxford, Oxfordshire, OX2 0ES, UK*

**This paper presents the results from a series of hypersonic double cone experiments, conducted in the X3 expansion tunnel at the University of Queensland (UQ). The model was previously used and produced at California Institute of Technology (Caltech) and is a scaled model of the double cone model used by the Calspan-University of Buffalo Research Center (CUBRC). The data presented is a full transient set of surface heat flux, and surface pressure measurements along the axial length of the model as well as a full suite of tunnel data. These aim to help characterize the flow over the geometry by providing surface conditions, an accurate location of the boundary layer separation, the flow reattachment points and the general structure of the shockwave boundary layer interaction. The geometry of the X3 facility is also provided to give a more complete picture of the test conditions, an important consideration for numerical models. The outcome of this paper is to provide the most detailed experimental data to date and improve validation attempts of existing non-equilibrium thermochemistry codes.**

## I. Nomenclature

$a$	=	Free stream speed of sound $\text{m.s}^{-1}$
$h_0$	=	Total enthalpy $\text{J.kg}^{-1}$
$h_w$	=	Wall enthalpy $\text{J.kg}^{-1}$
$h_\infty$	=	Free stream static enthalpy $\text{J.kg}^{-1}$
$M_\infty$	=	Free stream Mach number
$n_{fl}$	=	Number of flow lengths of gas until steady Pitot conditions
$P_{CT}$	=	Compression tube pressure Pa
$P_{DT}$	=	Dump tank/acceleration tube pressure Pa
$P_{Pitot}$	=	Pitot pressure Pa
$P_{Pitotex}$	=	Average experimental Pitot pressure Pa

---

\*D.Phil Candidate, Department of Engineering Science, Oxford Thermofluids Institute.

†Research Associate, Department of Engineering Science, Oxford Thermofluids Institute.

‡ARC DECRA Fellow, Centre for Hypersonics, School of Mechanical and Mining Engineering, AIAA Senior Member.

§PhD Candidate, Centre for Hypersonics, School of Mechanical and Mining Engineering.

¶Professor, Centre for Hypersonics, School of Mechanical and Mining Engineering. Associate Fellow AIAA.

|| Professor of Aerospace, Graduate Aerospace Laboratories, 1200 E. California Blvd, MC 105-50, Associate Fellow AIAA.

\*\*Associate Professor, Institute of Advanced Engineering and Space Sciences. Member AIAA.

††Associate Professor, Department of Engineering Science, Oxford Thermofluids Institute.

$P_{Res}$	=	Reservoir pressure Pa
$P_{static\infty}$	=	Free stream static pressure Pa
$P_{ST}$	=	Shock tube pressure Pa
$P_0$	=	Total pressure Pa
$\dot{q}$	=	Wall heat flux $W.m^2$
$Re_c$	=	Reynolds number behind the primary conical shock wave
$Re_{u_c}$	=	Unit Reynolds number behind the primary conical shock wave $m^{-1}$
$Re_{u\infty}$	=	Free stream unit Reynolds number $m^{-1}$
$Re_\infty$	=	Free stream Reynolds number
$St_c$	=	Stanton number calculated with post primary conical shock wave properties
$St_\infty$	=	Stanton number calculated with free stream properties
$T_\infty$	=	Free stream temperature K
$U_{s1}$	=	shock tube shock wave speed $m.s^{-1}$
$U_{s2}$	=	Acceleration tube shock wave speed $m.s^{-1}$
$u_c$	=	Flow velocity behind the primary conical shock wave $m.s^{-1}$
$u_\infty$	=	Free stream velocity $m.s^{-1}$
$\rho_c$	=	Density behind the primary conical shock wave $kg.m^{-3}$
$\rho_\infty$	=	Free stream density $kg.m^{-3}$

## II. Introduction

The double cone geometry has been used in various test cases for several years now, ranging from use exploring the effects of indented ablated nose tips [1], exploring real gas effects and more. The model used for the experiments presented in this paper was derived from the model first used by Holden et al. [1] as a validation test case for numerical codes. However, the flow a phenomenon created by this geometry is also applicable to the real world in locations where compression corners would exist such as control surfaces. While the general shock structure is analogous to a ‘Type VI’ shock interference case [2], the compression corner causes flow separation at high enthalpies in the corner region which produces both separation and reattachment shocks making a complicated flow structure. This produces larger variations in the heat flux and surface pressure along the surface of the geometry with peak values occurring in the region of flow reattachment. Any future attempts at designing hypersonic vehicles would greatly benefit from the full understanding and capability to predict flow properties on these features, thus there is a real-world motive for this test case considering the geometry alone.

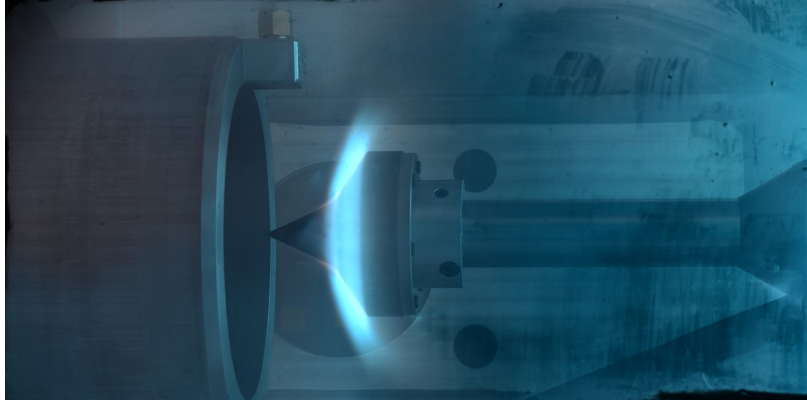


**Fig. 1 Double Cone model during test shot in the T6 tunnel at the University of Oxford.**

There have since been multiple experimental sets by the group at Calspan-University of Buffalo Research Center (CUBRC) [3, 4], which found cases run in nitrogen test gas proved successful in validation attempts by numerical modellers. However, in air environments, predictions showed poor agreement in higher enthalpies particularly for the prediction of the size of the separation region. Subsequent tests in pure oxygen environments showed similar results to the air cases with spectroscopy showing poor agreement with the level of nonequilibrium thermochemistry predicted in the free stream [4]. This was addressed by switching the experimental methods from reflected shock tunnel (LENS I) to

an expansion tube (LENS XX) where the level of nonequilibrium in the freestream would be less due to the principals of operation of expansion tubes. This led to the latest data set to be released by the group at CUBRC presented in [4].

Further prediction attempts completed [5–8] still show difficulties in predicting the flow separation lengths with attempts of uncertainty analysis [9] also completed to try and reach a conclusion. There are further datasets that were added to the mix such as the work conducted at Caltech T5 by Knisley and Austin [10], and the experiments at the Arnold Engineering Development Center (AEDC) tunnel no. 9 [11]. The tunnel no. 9 experiments are of interest as they describe unstable flow behaviour throughout the test time.

With the preceding work showing difficulties in the accurate prediction of flow properties, it shows further work is necessary to fully understand the problem. The aim of the work presented in this paper is to provide a complete transient dataset for the research community to use to improve the code validation attempts. One of the largest improvements on previous data sets is the addition of details of the X3 facility, shock speed history and the temporal variation of the measurements throughout the test time. It is also believed by the authors, that significant uncertainties surrounding the flow processes inside expansion tube facilities and the resultant flow produced. A secondary objective of this paper is to present initial data to be used to develop further understanding on the fundamentals of the facilities going forward.

### III. Experimental setup

#### A. Experimental Test Facility

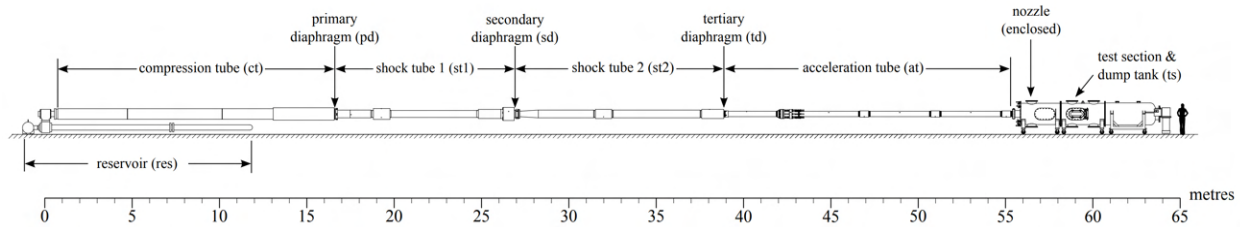


**Fig. 2 Schematic of X3 in expansion tube mode from Stennett et al. [12]**

Figure 2 shows the layout of X3 in the expansion tunnel mode for this test campaign. The development of X3 by Prof. R. G. Morgan began in 1994 with the first commissioning shots fired in 2001. For a detailed summary of the history X3 the reader is directed to Gildfind et al. [13]. The compression tube was separated from the shock tubes via a stainless steel primary diaphragm at the ‘primary diaphragm station’ of a thickness and score depth dependent on the desired rupture pressure. Both shock tubes 1 and 2 were used as one large shock tube filled with zero air as the primary test gas. Finally, the acceleration tube and dump tank formed a large continuous volume that was evacuated via vacuum pumps to a desired pressure. The acceleration tube and shock tube separated by a  $13\text{ }\mu\text{m}$  Mylar secondary diaphragm located at the ‘tertiary diaphragm station’ shown on Figure 2. The Mylar thickness was chosen to be as thin as a practically possible to mitigate the chance of model surface damage post rupture. An example of this effect can be seen in the work by James et. al [14].

In 2015, the X3 facility began development to incorporate a reflected shock tunnel (RST) mode of operation within its capability skill set to become a dual mode facility. This development saw modification to X3 including the re-boring of the second shock tube (st2) to 200 mm internal diameter, equal to shock tube 1. The acceleration tube has remained at the original 182.6 mm diameter meaning there is an area reduction from 200 mm to 182.6 mm at the interface between the shock tube and acceleration tube. Prior to the re-boring, there was an area increase at this same location. The effect of the area reduction on the test flow is unknown at this stage but a ramp section has been installed at this interface to avoid an abrupt change and therefore mitigate any effect that could be present. However, it is likely the presence of this area reduction serves to increase the uncertainty in the flow conditions by a significant amount. During this period of modification, the tunnel was relocated to a new site owned by the Department of Defence, Science and Technology (DST) in Brisbane, Australia giving it significantly more space to operate.

The current facility geometry including the area reduction at the secondary diaphragm used for this test campaign is presented in Figure 3. Due to the aspect ratio of the plot, the tunnel profile presented in Figure 3 exaggerates the area reduction to look almost like a forward-facing step. However, in reality the reduction occurs via a slope of approximately  $6.3^\circ$ .

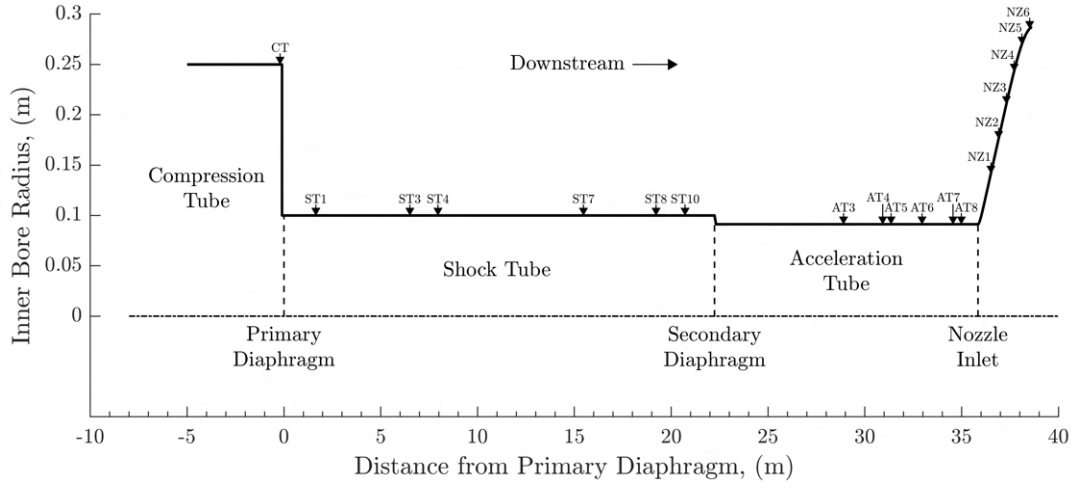


**Fig. 3 Inner bore geometry of X3 for double cone campaign.**

The end of the acceleration tube was terminated with a nozzle designed by Toniato et al. [15] reproduced here in Figure 4. This served to expand the flow further to attain the desired free stream conditions and increased the diameter of the core flow, allowing the model to be placed off the centre axis of the nozzle. This increased the survivability of the model by avoiding some fragmentation produced by the diaphragms at the point of rupture. The reader is encouraged to refer to Toniato et al. [15] for full details of the Mach 12 nozzle dimensions to form the foundation of any numerical facility rebuild.

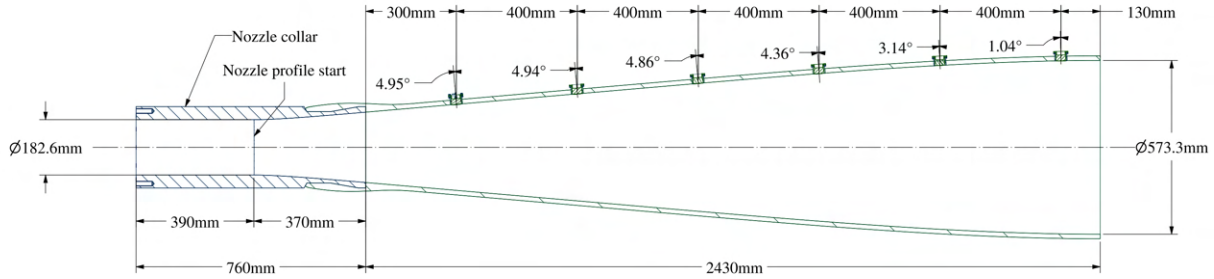


**Fig. 4 X3 Mach 12 Nozzle replicated from Toniato [16]**

Figure 4 also shows piezoelectric pressure transducers spanning the length of the nozzle at 400 mm intervals. These sensors are common to shock tubes in general and lined the full length of the tunnel from the primary diaphragm to allow shock speed to be calculated at different locations as the shock propagates through the tunnel from the initial primary diaphragm rupture. The position of the sensors are shown in Figures 3 and 4 with their precise locations presented in the appendix in Table 4 as a function of distance measured from the primary diaphragm.

#### IV. Double Cone Model

Figure 5 shows the geometry of the model used for this campaign. This model was developed by Caltech and represents a scaled model of the double cone model presented by Maclean et al. [5]. The model is equipped with 64 Type En-Kn hybrid coaxial thermocouples (TC) produced by Caltech based on the design by Sanderson and Sturtevant [17]. As a slight deviation from the design, the cold junction is formed at the back face of the thermocouple which was satisfactory for these short duration experiments. The model is also equipped with 10 XCS-062-25A Kulites along the surface of the model with custom protective screens to mitigate risk of damage from debris in the flow.

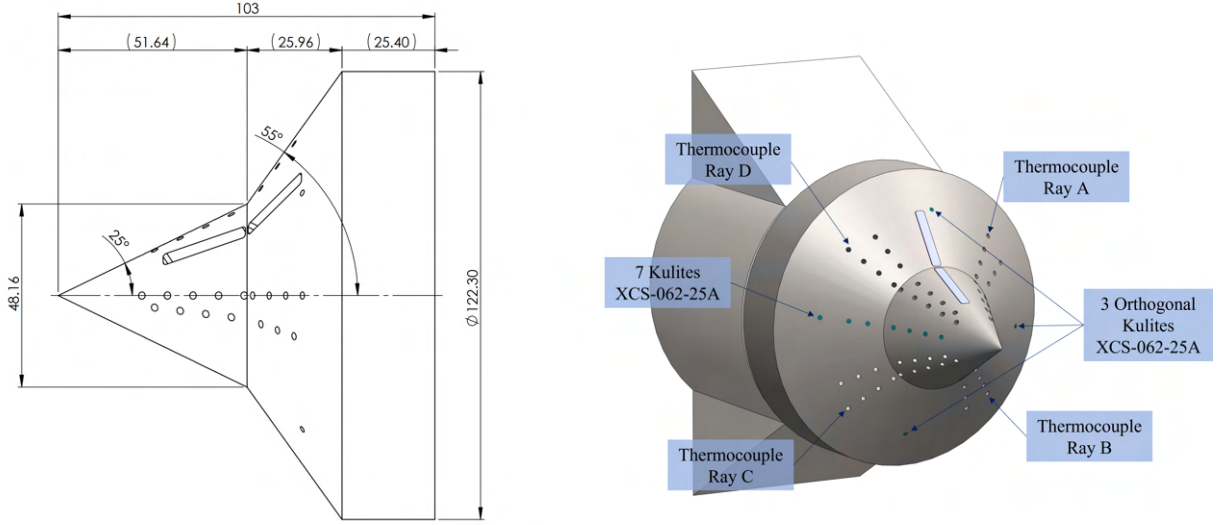


**Fig. 5 Dimensions of the double cone model and the sensor modifications are displayed. Dimensions are displayed in (mm).**

The 64 thermocouples are distributed in to four orthogonal arrays (A, B, C and D) labelled on Figure 5 to give a complete picture of the surface heat flux on the model and to give an insight in to any asymmetry in the flow. Each ray is split in to two further rays with a 15° separation. This is done purely to allow an increased density of sensors along the axial length of the model. This leads to a higher resolution of heat flux points plotted with axial distance. However, due to the reduced scale in comparison to the model used by Maclean et al. [5], the number of sensors that can be accommodated in the axial direction is limited and hence the resolution achieved is not as good as the resolution achieved in the CUBRC dataset.

A series of ‘onboard’ DAQ modules were used to record the sensors inside the test section at a rate of 1 MHz with a band width of 500 kHz. The data was then downloaded from the DAQ modules post-test to be processed. Not being a standard thermocouple type, the conversion from raw voltage to temperature was done with a custom reference used by Knisely and Austin (A. M. Knisely, personal communication, 25th Jul 2022). This used the difference in emf values for each ‘En’ and ‘Kn’ element vs platinum from the ASTM E230/E230M-17 tables to create a reference table for the emf between the En-Kn elements. The output temperature was then interpolated from the table. This showed satisfactory results and hence was used to convert the data for the double cone campaign in X3. The temperature signals were then converted to heat flux using Oldfield’s impulse response method [18] with a thermal product of  $9875.41 \text{ J.m}^{-2}.\text{K}^{-1}.\text{s}^{-0.5}$ . The output heat flux had considerable noise and so digital filtering was used to mitigate this effect. For condition X3-A, a lowpass filter with a cut-off frequency set to 20 kHz was used in conjunction with a 20-point moving average filter (applied internally in the temperature to heat flux conversion function) to extract a signal. For condition X3-B, the signal to noise ratio was lower and so required a 5 kHz filter in conjunction with a 50-point sample moving average filter to extract a suitable signal. The Kulite signals were subject to less noise than the thermocouples and so a low-pass filter with a 100 kHz frequency cut off was used.

The heat flux was converted to Stanton number ( $St$ ) to allow comparison of the data with the CUBRC data and others going forward. In this campaign,  $St_c$  was calculated by the following:

$$St_c = \frac{\dot{q}}{\rho_c u_c h_0} \quad (1)$$

Where the  $h_w$  is neglected due to  $h_0 \gg h_w$ . To calculate the free stream component  $St_\infty$ , the post primary conical shock values  $\rho_c u_c$  are switched for their free stream equivalents ( $\rho_\infty u_\infty$ ).

The configuration of the model mounting, and instrumentation is displayed in Figure 6. This depicts the double cone model mounted approximately 75 mm above the centreline of the nozzle to reduce the chance of debris impacting the model. At this height the bottom surface of the cone was still visible to the side circular windows of the test section used for attempting schlieren. The sensor cables were located inside the steel ‘L bracket’ and fed into the electronics



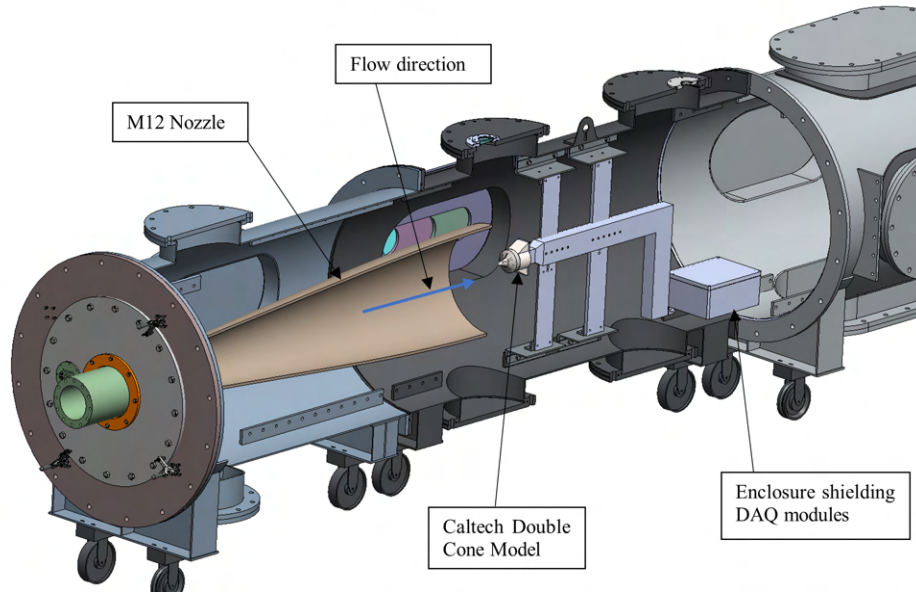
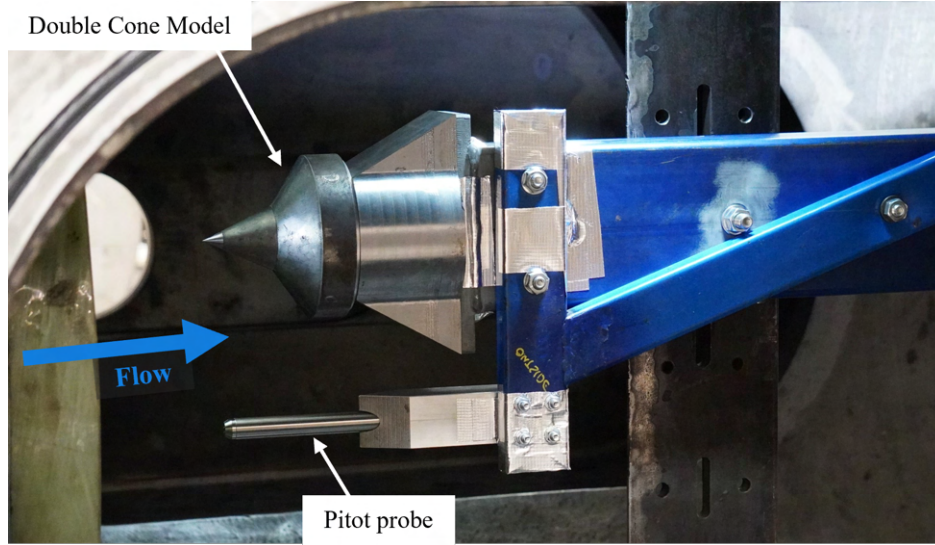


**Fig. 6** X3 Double Cone Model inserted in the X3 test section. A single Pitot probe can also be seen mounted below.

enclosure, home to 11 custom DAQ modules. A single custom Pitot probe offset equidistance below the centreline to the model nose tip was added to provide free stream Pitot pressure measurements simultaneously to the model data during test time. This gives an excellent opportunity to compare model data directly with the free stream conditions of individual shots rather than relying on Pitot probe free stream data from a previous Pitot rake campaign.

## V. Experimental Test Conditions

### A. Facility Flow Conditions

Table 1 shows the two target conditions from Maclean et al. [5] that were used in this campaign. Due to the scaled down model, the aim was to match the Reynolds number ( $Re_c$ ) behind the primary conical shock flowing into the double cone's compression corner while achieving a similar total enthalpy. The characteristic dimension for this used was the base diameter of the forward cone at the compression corner itself (48.16 mm as seen on Figure 5) . Since the

geometry is not a perfect scale model of the CUBRC cone due to manufacturing tolerances, the forward cone base diameter was the suitable choice representing the dimension with the most significance in this instance.

**Table 1 Reproduced table of target free stream conditions from Maclean et al. [4]**

Condition	Facility	$\rho_\infty$ $kg.m^{-3}$	$u_\infty$ $m.s^{-1}$	$T_\infty$ $K$	$Re_{u_\infty}$ $10^6 m^{-1}$	$h_0$ $MJ.kg^{-1}$	$M_\infty$	$P_{pitot}$ $kPa$
CUBRC Run 01	LENS-XX	$4.99 \times 10^{-4}$	3246	175	0.14	5.44	12.2	5.1
CUBRC Run 04	LENS-XX	$9.64 \times 10^{-4}$	6497	652	0.2	21.77	12.82	39.5

Equilibrium calculations, along with the characteristic dimension were used to estimate the post-primary-conical-shock  $Re_c$  from LENS XX CUBRC Run 04 as  $Re_c = 25373$ . The experimental X3  $Re_c$  was gained by calculating the post-primary-conical-shock properties, via a modified version of UQ's 0D state to state solver PITOT version 3 [19] to get  $Re_{uc}$  for a  $25^\circ$  cone. Then the characteristic dimension was applied to compare the  $Re_c$ . This comparison along with the calculated free stream conditions for each test are shown at the bottom of Table 2. Due to the limited knowledge and data from the CUBRC facility, this was the best estimate for flow condition matching.

**Table 2 Shot conditions from the X3 double cone campaign.**

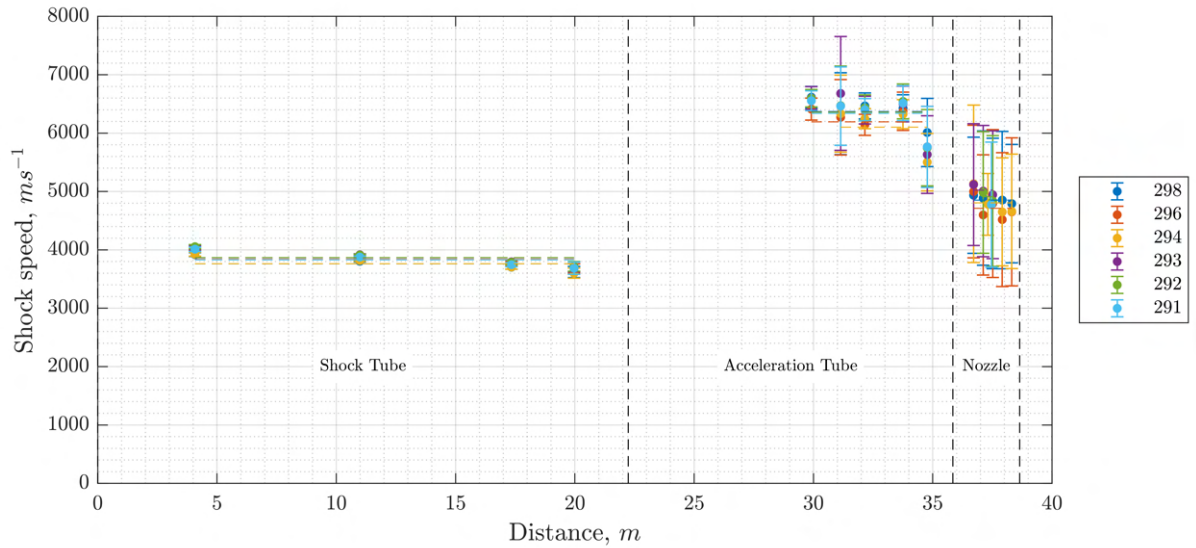
Shot number	291	292	293	294	296	298	300
Condition	X3-A	X3-A	X3-A	X3-A	X3-A-N2	X3-A	X3-B
Orifice Plate $\phi$ , (mm)	113	113	113	113	113	113	159.2
Driver Gas	100% He	100% He	100% He	100% He	100% He	100% He	100% N <sub>2</sub>
Test Gas	Zero Air	Zero Air	Zero Air	Zero Air	Nitrogen	Zero Air	Zero Air
Material	304 SS B2	304 SS B2	304 SS B2	304 SS B2	304 SS B2	304 SS B2	304 SS B2
Thickness/Score Depth, (mm)	1.2/0.2	1.2/0.2	1.2/0.2	1.2/0.2	1.2/0.2	1.2/0.2	0.9/0.25
$P_{Res}$ (kPa)	5515	5535	5496	5525	5511	5530	3465
$P_{CT}$ (kPa)	49.88	49.21	49.66	49.66	49.93	49.85	70.75
$P_{ST}$ (kPa)	4.01	4.05	3.98	4.06	4.17	4.03	3.27
$P_{DT}$ (Pa)	35.28	35.60	35.72	35.36	35.66	35.33	19.79
$P_{Pitot_{ex}}$ (Pa)	54397	52934	60902	37487	39621	58154	14761
$U_{s1}$ (m.s <sup>-1</sup> )	3865	3902	3903	3806	3850	3777	-
$U_{s2}$ (m.s <sup>-1</sup> )	6474	6516	6490	6274	6282	6453	-
$P_{static_\infty}$ (Pa)	471.02	489.23	488.11	429.00	396.33	451.78	-
$T_\infty$ (K)	1509.7	1552.3	1559.5	1421.8	1190.0	1417.5	-
$a$ (m.s <sup>-1</sup> )	752	761	763	731	672	730	-
$u_\infty$ (m.s <sup>-1</sup> )	6551.4	6609.0	6601.1	6498.8	6292.4	6398.8	-
$M_\infty$	8.72	8.68	8.65	8.89	9.36	8.77	-
$\rho_\infty$ (kg.m <sup>-3</sup> )	$1.09 \times 10^{-3}$	$1.10 \times 10^{-3}$	$1.09 \times 10^{-3}$	$1.05 \times 10^{-3}$	$1.16 \times 10^{-3}$	$1.11 \times 10^{-3}$	-
$P_{Pitot}$ (kPa)	45.5	46.8	46.3	43.3	44.7	44.3	-
$P_0$ (MPa)	270.09	282.68	275.02	272.70	299.69	242.27	-
$h_0$ (MJ.kg <sup>-1</sup> )	22.81	23.25	23.20	22.36	20.77	21.71	-
$h_\infty$ (MJ.kg <sup>-1</sup> )	1.35	1.41	1.42	1.25	0.97	1.24	-
$Re_{u_\infty}$ (m <sup>-1</sup> )	123763	123783	122411	123584	148723	128804	-
$Re_{uc}$ (m <sup>-1</sup> )	505317	512814	508010	491045	533413	505568	-
$Re_c$	24335	24696	24465	23648	25688	24347	-
Error $Re_c$ w.r.t. CUBRC	-4.09%	-2.67%	-3.58%	-6.80%	1.24%	-4.04%	-

Table 2 shows the actual tunnel fill conditions and calculated flow properties achieved for each of the shots. As can be seen there are 6 shots presented for condition X3-A and only one for condition X3-B. The reason for this is there was significant work between shots attempting to capture quality schlieren at this condition. Iterations in the setup between shots led to numerous shots at the same target conditions which serves to increase the pool of data available to the community. A single shot at condition X3-A with a pure nitrogen test gas is also presented (shot 296). This was

completed due to challenges with radiation from the flow saturating the schlieren images. However, this extra shot remains to extend the dataset. The free stream conditions for condition X3-B (shot 300) have not been calculated due to challenges with the modified PITOT code at this condition. This is planned to be addressed, but the respective facility conditions remain to allow and encourage the community to calculate their own free stream conditions for all shots.

## B. Shock Speed History

One of the main objectives of this paper was to provide a full data set including the facility data. Figure 7 shows all shock speed profiles from condition X3-A shots displayed in Table 2. There are three sections shown namely the shock speeds in the shock tube, acceleration tube and the M12 expansion nozzle. The points represent a simple distance by time calculation for the average shock speed between two sensors. Figure 7 shows all shots showing a broadly similar profile with the initial shock wave decelerating through the shock tube between  $3500\text{--}4000\text{ m.s}^{-1}$ . Next the shock ruptures the secondary diaphragm and is accelerated through an unsteady expansion shown in Figure 7 around  $6500\text{ m.s}^{-1}$ . At the end of the acceleration tube the shock decelerates as it is expanded through the nozzle. The error bars on the graph represent an uncertainty of when the shock arrived. This is calculated via a selection of the points before and after the user is confident each shock arrived. For instance, the first point where pressure is deemed to be rising due to the shock wave, and the point where the initial step in pressure has concluded from the shock wave passing. Since the pressure transducers measure the pressure in the boundary layer along the tunnel wall, not the shock directly, the possibility of determining the exact instant the shock arrived can be remote. The nozzle wall sensors are a prime example due to the dilated response of the sensors during the steady expansion. With the uncertainty in the exact arrival time of the shock wave per sensor, this allows the maximum and minimum average shock speeds between the shock speeds to be calculated, hence the error bars.



**Fig. 7 Condition X3-A shock speed histories.**

The shock speeds are important as this directly impacts the state of the gas being processed, that has a knock-on effect in the following processes leading up to the free stream. This was found by Collen et al.[20] who found the shock history had an influence of the overall properties of the free stream gas. From Figure 7 the shock speed appears to be decelerating almost linearly along the shock tube, meaning each infinitesimally small slice of gas will be processed by a shock wave with a different speed. This is likely to give a continuously varying set of properties of the test gas along the tunnel post shock which goes on to feed the free stream flow. The shock speeds presented here along with the tunnel geometry and fill conditions gives the numerical modelling community an opportunity to calculate more accurate free stream flows from each shot, which can then be fed as an input to a second numerical model of the double cone for an enhanced assessment of the numerical codes.



### C. Facility Test Time

An important part these tests is analysing the data to determine the test time in which we can use to analyse the results. This is usually done during a condition development campaign with a dedicated Pitot rake. However, in this case we can use the sensors on the model, and the single Pitot probe to get a good idea of the facility test time.

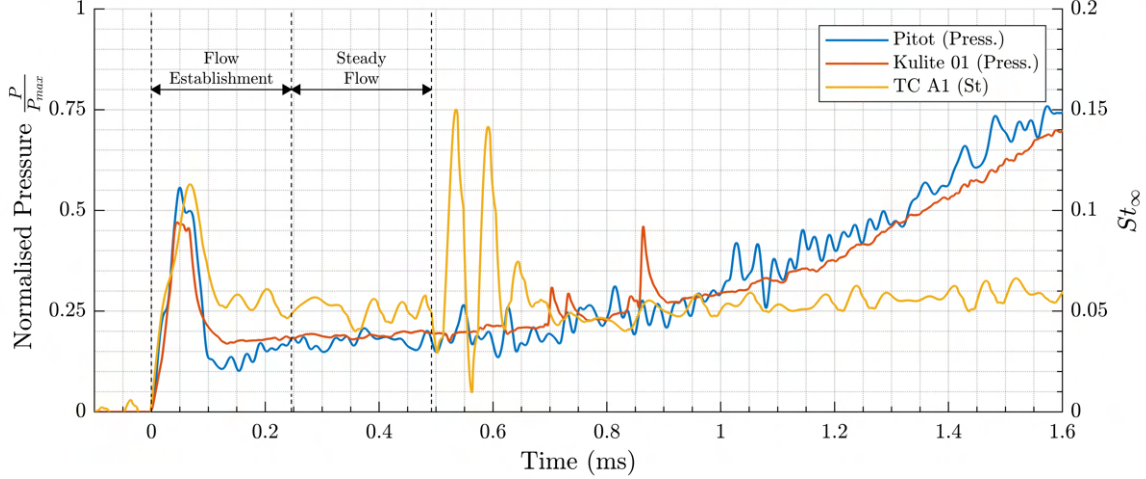


**Fig. 8 Condition X3-A (shot 294) Transient data showing the estimated test time of the trace.**

Figure 8 shows the transient traces of three sensors (Pitot probe, Model Kulite 01 and Model TC A1) for shot 294 condition X3-A. These sensors have been time aligned, where zero marks the point of flow arrival at each sensor and the pressures normalised to the max value in the sample set to allow direct comparison. The thermocouple response has been nondimensionalised to Stanton number. Initially at the flow arrival, there is a peak in all three sensors as the shock and acceleration gas pass over the model. The thermocouple and model Kulite drop to a steady level where the thermocouple appears to have a slight negative gradient and the model Kulite a slight positive gradient. However, the Pitot sensor drops further and has a slightly stronger positive gradient, rising to a reasonably stable value at approximately 0.25 ms. This transient period is marked as the ‘flow establishment’ region and is a similar case for the other shots in condition X3-A. Immediately following this period, the three sensors enter a stable state with little change in magnitude. At approximately 0.492 ms, the thermocouple has a larger transient response the cause of which isn’t clear. Although the Pitot and model Kulite traces continue to look steady, the digital filters removed some high frequency noise from these traces that starts at a similar time to the transient thermocouple response. For this reason, the suggested steady flow region is indicated in Figure 8 as occurring between 0.246-0.492 ms giving a steady period of 246  $\mu$ s. If the thermocouple trace is neglected, the steady region appears to have the capability to go further until approximately 0.7 ms before the pressure in both the Pitot and model Kulite begin to rise.

**Table 3 Suggested times of steady flow periods, their duration, and the number of flow lengths to achieve steady flow from shock arrival for each shot.**

Shot	$t_{start}$ ms	$t_{period}$ ms	$n_{fl}$
291	0.316	0.16	414
292	0.334	0.131	441
293	0.501	0.203	661
294	0.246	0.246	320
296	0.182	0.308	229
298	0.359	0.143	459
300	0.838	0.936	-

A table of suggested steady period start times w.r.t. flow arrival and period duration for each shot is shown in Table 3. Where  $t_{start}$  is the estimated start time of the steady period for each shot,  $t_{period}$  is the duration of steady flow, and  $n_{fl}$  is the number of flow length required to reach the start of the steady period.  $n_{fl}$  is calculated by calculating the effective slug length of gas during flow establishment and dividing by an assumed separation bubble length of 5 mm.

## VI. Results

### A. Test Time Averaged Double Cone Results

Figure 9 shows the surface distributions of the Stanton number and the ratio of surface pressure to free stream Pitot pressure, averaged over an estimated steady bubble period. The  $x$  axis is the ratio of the sensor's axial location w.r.t. the nose tips and the axial length of the forward cone. As mentioned previously the cones are not perfect scale models and so this ensures the distances are comparable with a common reference to the compression corner at 1 unit of distance. The pressure ratio was used with average experimental Pitot pressure to scale the values back to a comparable metric by relating them to the respective free streams. The lines between the data points are used to assist with observing general trends and do not indicate/represent the values between data points.

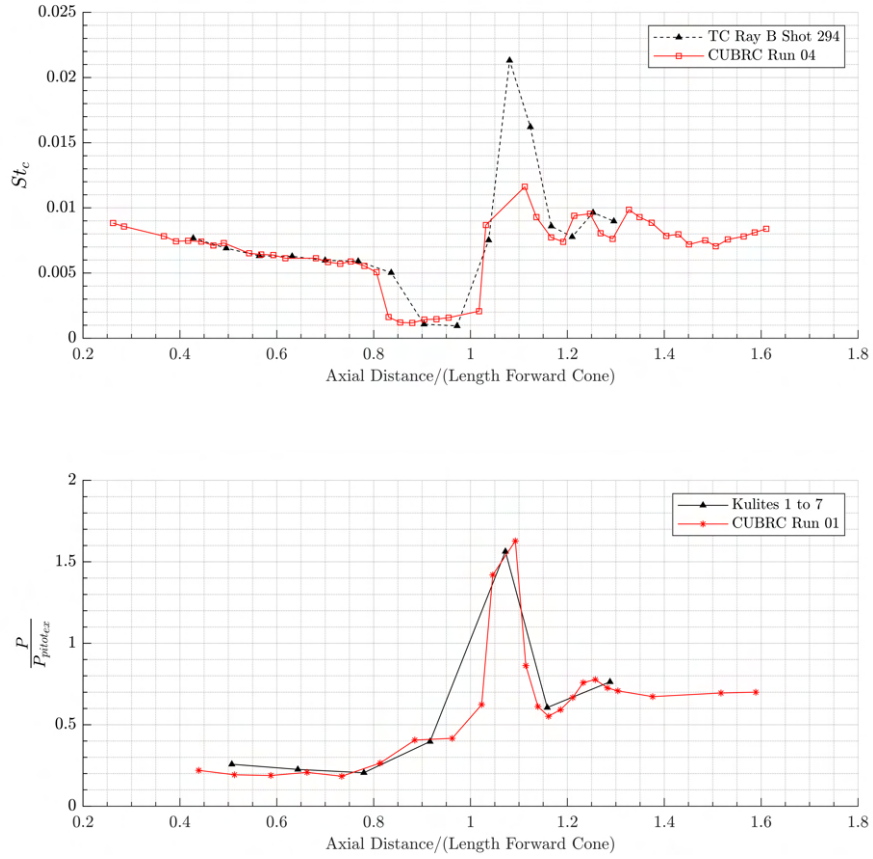


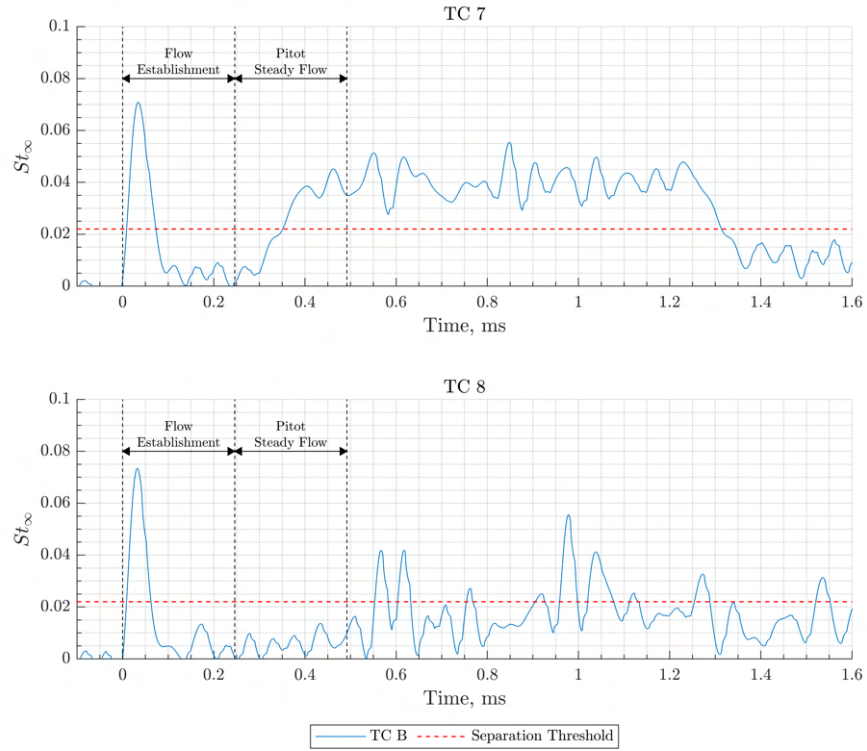
**Fig. 9 Condition X3-A (shot 294) time averaged  $St_c$  and pressure comparisons to CUBRC Run 04.**

As a general overview, the comparisons of the X3 data and CUBRC data look very good with the magnitudes of the  $St_c$  and pressure ratio being almost identical in the section prior to the separation bubble. Also considering the flow just after reattachment, when the peak values drop to a steady level, the traces for both data sets continue to look very comparable. However, there appears to be a difference in the size of the separation bubble, perhaps more noticeable on the Stanton number graph in Figure 9. The CUBRC data shows a larger separation bubble by at least 0.05 axial units from the compression corner. This translates to a bubble deficit of 2.6 mm on the X3 double cone model, or at least 5% difference between the two. It's a similar story for the pressure ratio comparison although less obvious due to the

reduced resolution of both datasets. Another large difference is the peak values achieved. Particularly for  $St_c$  where the peak value for the CUBRC data is approximately half of the peak value on shot 294 ray B. Again, there is reduced resolution in this area of peak heat transfer meaning the actual peak values are not fully resolved.

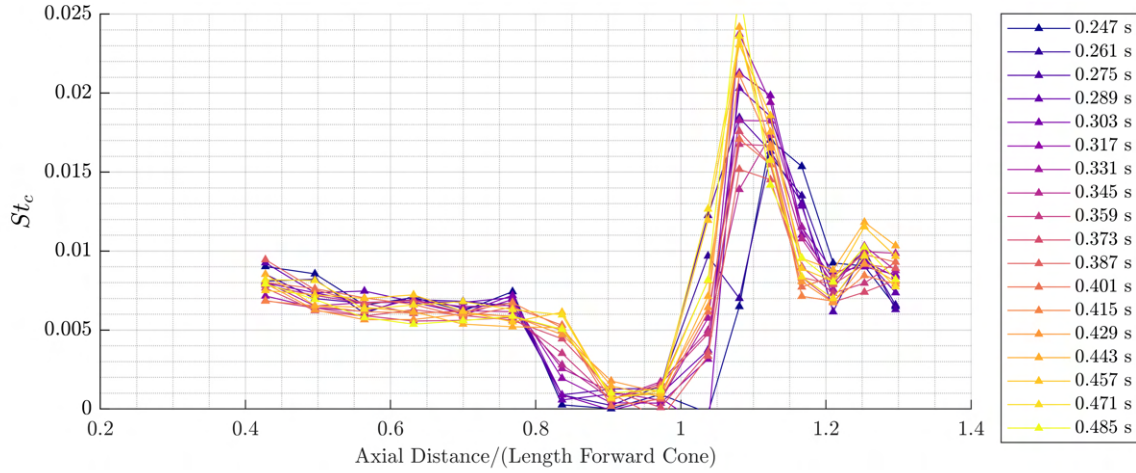
## B. Transient Double Cone Results

A key objective for this campaign was to present an insight into the transient behaviour of the flow on the double cone model. For instance, providing evidence if the data is truly steady state or not. It's already been noted for the pitot trace and a couple of model sensors in Figure 8 that suggests there is a period of steady flow supplied to the model. Furthermore, in the areas furthest upstream on the model surface, this steady flow is also seen. To assess this, the separation bubble size was calculated forward of the compression corner on the double cone model for each instant in time. The bubble size is determined via a simple script that loops through the first nine thermocouples for a given ray and applies a conditional statement at each instant in time to determine if the  $St_\infty$  has fallen below a defined threshold. For condition X3-A, an appropriate threshold was determined to be  $St_\infty = 0.022$ .



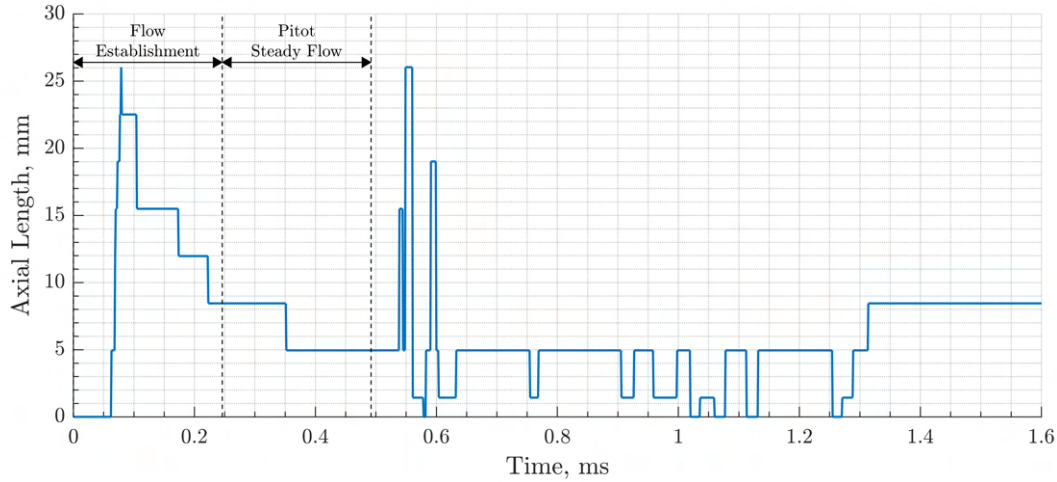
**Fig. 10 Condition X3-A (shot 294) transient thermocouple traces displaying the threshold separation condition.**

Figure 10 shows the threshold in action graphically and includes the same periods of steady supply flow labelled from Figure 8. Looking at TC 7 from Figure 10,  $St_\infty$  has the same characteristic peak seen previously as the flow arrives before dropping to  $St_\infty = 0.01$  below the threshold. This indicates that initially during the flow establishment period, the separation bubble passes further upstream than TC 7. After this initial period, there is a rise in TC 7's  $St_\infty$  from 0.3 ms onwards. This rise in  $St_\infty$  goes above the threshold and indicated the separation region was shrinking downstream towards the compression corner. However, there's no indication in TC 8 of any change in state locally. Therefore, this suggests that initially there is a large separation bubble that forms during the initial stages of the flow that then shrinks to a possible steady bubble size. Also like shown previously, in Figure 8, after the end of the labelled steady pitot period, there is the same disturbance on TC 8 that starts a period where it is difficult to determine if the flow has remained separated. Given that it has not risen back to the nominal value of approximately  $St_\infty = 0.04$  shown in TC 7, it would be reasonable to assume that it is still separated in some fashion. At 1.25 ms after the flow arrives at TC 7,  $St_\infty$  drops below the threshold again indicating the bubble is growing in conjunction with the rising free stream pressure.



**Fig. 11 Condition X3-A (shot 294) surface heat flux distributions with time on thermocouple ray (Ray B).**

Figure 11 shows the  $St_c$  distribution at different snapshots in time within the steady pitot time period defined previously. At each increasing increment in time, the colour of the markers and lines get lighter allowing a visualisation of how the heat transfer develops and how the size of the bubble develops. This shows that for the period of the steady Pitot pressure, the separation bubble shrinks indicated by the rise in  $St_c$  at TC 7 (approximately 0.84 units along the length of the cone). This highlights the importance of defining a test time for the purpose of calculating an average bubble size. For instance Figure 11 shows that the period of steady Pitot pressure does not mean a steady bubble size. Hence the average distributions shown in Figure 9, were calculated based on an estimated steady bubble size, and not the steady Pitot period.



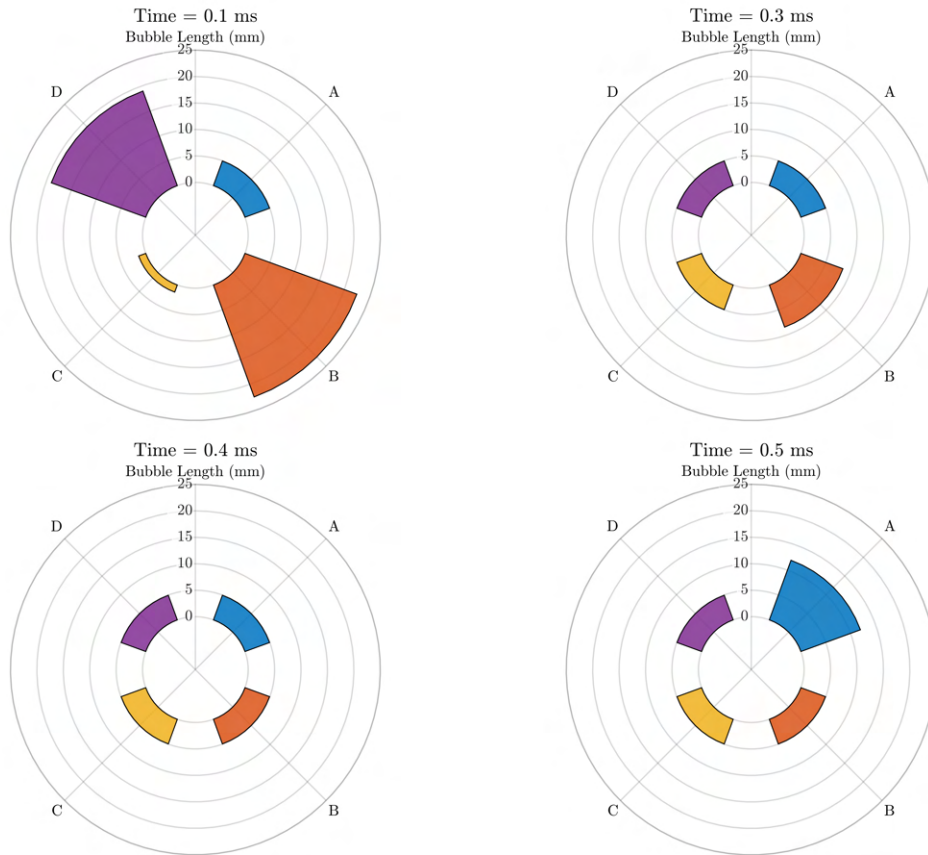
**Fig. 12 Condition X3-A (shot 294) separation bubble size time history on single thermocouple ray (Ray B).**

Figure 12 shows the estimated bubble size over the same periods as Figures 8 and 10, with the same labels indicating the steady Pitot pressure for convenience. The discrete bubble sizes are clearly shown by the 'stepped' profile as the bubble passes the thresholds on individual sensors in the ray. As described before, we can see in the initial stages after flow arrival, the formation of a large separation bubble almost measuring 26 mm in the axial direction. before shrinking back down to 5 mm and remaining steady. As mentioned previously the period of constant bubble size does not align with the steady Pitot period, suggesting a required development period before reaching a stable value. Also as before, we can see the impact of the disturbance on the sensors at approximately 0.54 ms where there are large spikes in the

indicated bubble size. However, this is not thought to be physical change in bubble size but a by-product of the unsteady signal rapidly spiking past the threshold caused by an unknown disturbance. After 0.65ms this region appears to show a steady bubble size but with noise causing jumps between the discrete bubble sizes. Finally, as seen in Figure 10, with the bubble growing past TC 7 from 1.25 ms, the same can be seen in Figure 12.

### C. Asymmetry Assessment of Data

An additional objective from this study was to address the axisymmetric assumption commonly used by the modelling community. Figure 13 shows the separation bubble on all four rays (Labelled A to D) at four snapshots in time from condition X3-A shot 294. The snapshots namely:  $t_1 = 0.1$ ,  $t_2 = 0.3$ ,  $t_3 = 0.4$ , and  $t_4 = 0.5$  ms can be referenced back to 12 for context of where the snapshots were taken in the bubble development process. The first ( $t_1$ ) is taken during flow establishment at 0.1 ms from flow arrival. Whereas  $t_2$  and  $t_3$  are taken during the supposed Pitot steady flow period, and  $t_4$  just after the Pitot period but just prior to the bubble spikes between 0.5 and 0.6 ms.



**Fig. 13 Condition X3-A (shot 294) separation bubble sizes across all rays at snapshots in the test time.**

At  $t_1$ , very significant non-axisymmetric bubble sizes 0.1 ms after flow arrival can be seen which corresponds the large start-up bubble at the beginning of the flow. This is when the bubble is shrinking towards a ‘steady’ size. The difference between the maximum and minimum axial bubble size is approximately 22 mm (between Rays B and C). This suggests the transient shrinking process is not an axisymmetric one and sets a precedent that the flow can be subject to large variations in bubble size in adjacent rays. At  $t_2$  the bubble is still in the shrinking phase referring back to Figure 12. However, compared to  $t_1$ ,  $t_2$  appears much more stable and almost axisymmetric, with rays A, C and D all having a separation bubble size of approximately 5 mm. At  $t_3$  (0.1 ms later), the snapshot shows for this shot, the bubble appears axisymmetric at this instant, or is at least between the resolution of the sensors. Finally, at  $t_4$ , rays B, C and D remain at approximately 5 mm whereas ray A indicates an increased separation bubble size. When looking at the raw data, this



increase appears to be related to the noise disturbance appearing in Figure 12 and others but at this instant affecting TC A6 more than the other sensors. This is a false indication of the separation bubble on this ray, as the immediately downstream sensor TC A7 shows no sign of separation at  $t_4$ . Therefore, it suggests the separation bubble size could be axisymmetric, at least between  $t_3$   $t_4$ , although having mentioned previously, this is limited by the low resolution in axial distance provided by the thermocouples. Given the difference between the axial location of the sensors is approximately 3.5 mm. for shot 294, the bubble size is therefore 5mm with a tolerance of  $\pm 3.5$  mm.

## VII. Conclusion

This paper presents a test campaign conducted in the X3 expansion tunnel for a series of transient double cone shots complete with data. The modifications to the X3 expansion tunnel have been highlighted along with the current geometry and positions of sensors showing the shock speed history in the tunnel for each shot. In addition, the fill conditions and free stream conditions have been provided to allow the numerical community to begin simulating the X3 double cone experiments starting on the facility side. Due to the quantity of experimental data collected, the authors will be making the data available in the near future in a separate more tangible format.

A single shot for condition X3-A (shot 294) was presented to attempt to answer various questions that inspired this campaign. The data appeared to show excellent agreement with the original CUBRC data for the time averaged  $St_c$ , although there were slight differences in the physical size of the bubble at the compression corner. With the transient data, the time history of the separation bubble size was shown giving an insight in the development of the bubble through the test time, which suggested there could be a region where the bubble remains at a steady size. However the resolution of the physical sensor spacing limits the ability to give an exact conclusion on this. In addition with the presence of 4 orthogonal rays, the test campaign shed light on the question of axisymmetry. The data suggested for certain periods of shot 294, that the flow was indeed axisymmetric. With data existing on numerous other shots yet to be fully analysed, further work to confirm that this result is repeatable across all of the tests should be done. From shot 294, it is clear that the test time definition is a very important factor which could influence these conclusions. A mistake in the selected test time could lead to a period of non-axisymmetric flow meaning different bubble size results at different locations on the cone. Therefore with the upcoming release of the transient data to the community, numerical models can be compared to the bubble size at both time averaged as well as different individual snapshots in time.



## Appendix

**Table 4** Locations of shock timing pressure transducers.

Distance From Primary Diaphragm	Sensor Name	Location
-0.201	CT	Compression Tube
0	-	Primary Diaphragm Station
1.649	ST1	Shock Tube 1
6.504	ST3	Shock Tube 1
7.955	ST4	Shock Tube 1
15.468	ST7	Shock Tube 2
19.217	ST8	Shock Tube 2
20.715	ST10	Shock Tube 2
22.237	-	Tertiary diaphragm Station
28.9	AT3	Acceleration Tube
30.925	AT4	Acceleration Tube
31.355	AT5	Acceleration Tube
32.955	AT6	Acceleration Tube
34.555	AT7	Acceleration Tube
34.984	AT8	Acceleration Tube
35.843	-	Nozzle Profile start
36.513	NZ1	M12 Nozzle
36.913	NZ2	M12 Nozzle
37.313	NZ3	M12 Nozzle
37.713	NZ4	M12 Nozzle
38.113	NZ5	M12 Nozzle
38.513	NZ6	M12 Nozzle
38.643	-	Nozzle Exit

**Table 5 Axial location of double cone thermocouple positions.**

TC No.	Axial Location w.r.t. nose tip
	mm
1	22.08
2	25.60
3	29.12
4	32.62
5	36.14
6	39.66
7	43.19
8	46.69
9	50.21
10	53.58
11	55.80
12	58.02
13	60.25
14	62.48
15	64.71
16	66.92

**Table 6 Axial location of double cone Kulite positions.**

Kulite No.	Axial Location w.r.t. nose tip
	mm
1	26.19
2	33.23
3	40.27
4	47.32
5	55.36
6	59.82
7	66.51

### Acknowledgments

I would like to give a huge thank you to Richard Morgan and Matthew Thompson from the University of Queensland for vital support for this campaign particularly with condition development and data processing. In addition I would also like to thank the staff at DST for hosting me and the stellar support they provided throughout this campaign, without which, this would not have been possible.

### References

- [1] Holden, M. S., Wadhams, T. P., Harvey, J. K., and Candler, G. V., "Comparisons between measurements in regions of laminar shock wave boundary layer interaction in hypersonic flows with navier-stokes and DSMC solutions," Tech. Rep. RTO-TR-AVT-007-V3, Aerothermal and Aero-Optics Evaluation Center, 2006.

- [2] Babinsky, H., and Harvey, J. K., *Shock wave-boundary-layer interactions*, Vol. 32, Cambridge University Press, 2011. <https://doi.org/10.1017/CBO9780511842757>.
- [3] Holden, M., Harvey, J., Wadhams, T., and MacLean, M., "A review of experimental studies with the double cone and hollow cylinder/flare configurations in the LENS hypervelocity tunnels and comparisons with Navier-Stokes and DSMC computations," *48th AIAA Aerospace Sciences Meeting Including the New Horizons Forum and Aerospace Exposition*, 2010, p. 1281. <https://doi.org/10.2514/6.2010-1281>.
- [4] MacLean, M., Holden, M. S., and Dufrene, A., "Measurements of real gas effects on regions of laminar shock wave/boundary layer interaction in hypervelocity flows," Tech. rep., CUBRC Inc., 2014. URL [https://www.cubrc.org/\\_iassets/docs/laminar-xx-paper.pdf](https://www.cubrc.org/_iassets/docs/laminar-xx-paper.pdf).
- [5] MacLean, M., Holden, M., and Dufrene, A., "Comparison between CFD and measurements for real-gas effects on laminar shock wave boundary layer interaction, I," *Oral Presentation, AIAA Aviation*, 2014. URL [https://cubrc.org/\\_iassets/docs/CUBRC\\_laminar\\_Atlanta.pdf](https://cubrc.org/_iassets/docs/CUBRC_laminar_Atlanta.pdf).
- [6] Candler, G. V., "Rate-dependent energetic processes in hypersonic flows," *Progress in Aerospace Sciences*, Vol. 72, 2015, pp. 37–48. <https://doi.org/10.1016/j.paerosci.2014.09.006>.
- [7] Hao, J., Wang, J., and Lee, C., "Numerical simulation of high-enthalpy double-cone flows," *AIAA Journal*, Vol. 55, No. 7, 2017, pp. 2471–2475. <https://doi.org/10.2514/1.J055746>.
- [8] Holloway, M. E., Chaudhry, R. S., and Boyd, I. D., "Assessment of hypersonic double-cone experiments for validation of thermochemistry models," *Journal of Spacecraft and Rockets*, Vol. 59, No. 2, 2022, pp. 389–400. <https://doi.org/10.2514/1.A35052>.
- [9] Kieweg, S. L., Ray, J., Weirs, V. G., Carnes, B., Dinzi, D., Freno, B., Howard, M., Phipps, E., Rider, W., and Smith, T., "Validation assessment of hypersonic double-cone flow simulations using uncertainty quantification, sensitivity analysis, and validation metrics," *AIAA SciTech 2019 Forum*, 2019, p. 2278. <https://doi.org/10.2514/6.2019-2278>.
- [10] Knisely, A. M., and Austin, J. M., "Geometry and test-time effects on hypervelocity shock-boundary layer interaction," *54th AIAA Aerospace Sciences Meeting*, 2016, p. 1979. <https://doi.org/10.2514/6.2016-1979>.
- [11] Coblish, J., Smith, M., Hand, T., Candler, G., and Nompelis, I., "Double-cone experiment and numerical analysis at aedc hypervelocity wind tunnel no. 9," *43rd AIAA Aerospace Sciences Meeting and Exhibit*, 2005, p. 902. <https://doi.org/10.2514/6.2005-902>.
- [12] Stennett, S. J., Gildfind, D. E., Jacobs, P. A., and Morgan, R. G., "Performance optimization of X3R: A new reflected shock tunnel mode for the X3 expansion tube," *2018 Aerodynamic Measurement Technology and Ground Testing Conference*, 2018, p. 3563. <https://doi.org/10.2514/6.2018-3563>.
- [13] Gildfind, D. E., Morgan, R. G., and Jacobs, P. A., "Expansion Tubes in Australia," *Experimental Methods of Shock Wave Research*, edited by O. Igra and F. Seiler, Springer International Publishing, Cham, 2016, pp. 399–431. [https://doi.org/10.1007/978-3-319-23745-9\\_13](https://doi.org/10.1007/978-3-319-23745-9_13).
- [14] James, C. M., Ravichandran, R., Smith, D. R., Cullen, T. G., and Morgan, R., "Scaled Apollo Capsule Heat Flux Measurements in the X3 Expansion Tube," *AIAA Aviation 2020 Forum*, 2020, p. 3278. <https://doi.org/10.2514/6.2020-3278>.
- [15] Toniato, P., Gildfind, D., Jacobs, P., and Morgan, R., "Expansion tube nozzle design using a parallel simplex algorithm," *Shock Waves*, Vol. 30, No. 2, 2020, pp. 185–199. <https://doi.org/10.1007/s00193-019-00930-2>.
- [16] Toniato, P., "Free-jet testing of a Mach 12 scramjet in an expansion tube," Ph.D. thesis, School of Mechanical and Mining Engineering, The University of Queensland, 2019. <https://doi.org/10.14264/uql.2019.342>.
- [17] Sanderson, S., and Sturtevant, B., "Transient heat flux measurement using a surface junction thermocouple," *Review of Scientific Instruments*, Vol. 73, No. 7, 2002, pp. 2781–2787. <https://doi.org/https://doi.org/10.1063/1.1484255>.
- [18] Oldfield, M. L. G., "Impulse Response Processing of Transient Heat Transfer Gauge Signals," *Journal of Turbomachinery*, Vol. 130, No. 2, 2008. <https://doi.org/10.1115/1.2752188>.
- [19] James, C., Gildfind, D., Lewis, S., Morgan, R., and Zander, F., "Implementation of a state-to-state analytical framework for the calculation of expansion tube flow properties," *Shock Waves*, Vol. 28, No. 2, 2018, pp. 349–377. <https://doi.org/10.1007/s00193-017-0763-3>.
- [20] Collen, P. L., Satchell, M., Di Mare, L., and McGilvray, M., "The influence of shock speed variation on radiation and thermochemistry experiments in shock tubes," *Journal of Fluid Mechanics*, Vol. 948, 2022, p. A51. <https://doi.org/10.1017/jfm.2022.727>.